

Solid-State ^{31}P and ^1H NMR Investigations of Amorphous and Crystalline Calcium Phosphates Grown Biomimetically From a Mesoporous Bioactive Glass

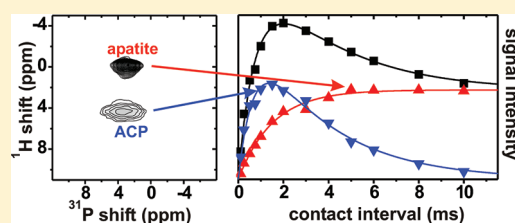
Renny Mathew,[†] Philips N. Gunawidjaja,[†] Isabel Izquierdo-Barba,^{§,||} Kjell Jansson,[‡] Ana García,^{§,||} Daniel Arcos,^{§,||} María Vallet-Regí,^{§,||} and Mattias Edén^{*,†}

[†]Physical Chemistry Division and [‡]Inorganic and Structural Chemistry Division, Department of Materials and Environmental Chemistry, Arrhenius Laboratory, Stockholm University, SE-106 91, Stockholm, Sweden

[§]Departamento de Química Inorgánica y Bioinorgánica, Facultad de Farmacia, Universidad Complutense de Madrid, 28040 Madrid, Spain

^{||}Networking Research Center on Bioengineering, Biomaterials and Nanomedicine (CIBER-BBN), Madrid, Spain

ABSTRACT: By exploiting ^1H and ^{31}P magic-angle spinning nuclear magnetic resonance (NMR) spectroscopy, we explore the proton and orthophosphate environments in biomimetic amorphous calcium phosphate (ACP) and hydroxyapatite (HA), as grown in vitro at the surface of a $10\text{CaO}-85\text{SiO}_2-5\text{P}_2\text{O}_5$ mesoporous bioactive glass (MBG) in either a simulated body fluid or buffered water. Transmission electron microscopy confirmed the presence of a calcium phosphate layer comprising nanocrystalline HA. Two-dimensional $^1\text{H}-^{31}\text{P}$ heteronuclear correlation NMR established predominantly $^1\text{H}_2\text{O} \leftrightarrow ^{31}\text{PO}_4^{3-}$ and $\text{O}^1\text{H} \leftrightarrow ^{31}\text{PO}_4^{3-}$ contacts in the amorphous and crystalline component, respectively, of the MBG surface-layer; these two pairs exhibit distinctly different $^1\text{H} \rightarrow ^{31}\text{P}$ cross-polarization dynamics, revealing a twice as large squared effective $^1\text{H}-^{31}\text{P}$ dipolar coupling constant in ACP compared with HA. These respective observations are mirrored in synthetic (well-crystalline) HA, and the amorphous calcium orthophosphate (CaP) clusters that are present in the pristine MBG pore walls: besides highlighting very similar local ^1H and ^{31}P environments in synthetic and biomimetic HA, our findings evidence closely related NMR characteristics, and thereby similar local structures, of the CaP clusters in the pristine MBG relative to biomimetic ACP.



1. INTRODUCTION

Biomaterialized tissues, such as bone and dentin, manifest a remarkable stability and stiffness, which is attributed to their heterogeneous organic/inorganic composite nature. The organic matrix mainly involves fibrous collagen and to a lesser extent (glyco)proteins and citrate,^{1–4} whereas the inorganic part constitutes Ca-deficient hydroxy-carbonate apatite (HCA; $\approx 3-9$ wt % carbonate), substituted with additional ions, for example, Na^+ , Mg^{2+} , and F^- .^{1,5}

Repairing bone/tooth defects or fractures demands an implant with the minimum requirement of biocompatibility, that is, that it is nontoxic and will not be expelled by the human body. Whereas the first generation of biomaterials was essentially “inert” (e.g., alumina and zirconia), more recently, “resorbable” and “bioactive” ceramics and glasses^{6–10} have found applications mainly in orthopedic, spine, and periodontal surgery. On contact with body fluids, they possess tissue-bonding abilities because of the formation of a biomimetic layer of amorphous calcium phosphate (ACP) that subsequently converts into nanocrystalline HCA. However, despite massive efforts for their elucidation, many details of these biomimetic processes remain largely unknown.

Whereas the composition, structure, and evolution of the biomimetic phosphate layer generated in vitro at the surface of bioactive glasses (BGs) have been addressed by a diversity of characterization techniques,^{11–23} primarily powder X-ray diffraction, electron

microscopy (EM) coupled to energy-dispersive X-ray (EDX) spectroscopy, and infrared and Raman spectroscopy, very few studies employed solid-state nuclear magnetic resonance (NMR).^{24–29} Yet, several structural investigations using ^1H and ^{31}P NMR spectroscopy are reported on naturally biomaterialized tissues, such as bone and tooth.^{3,4,30–42} However, whereas their inorganic phosphate content is substantial (≥ 60 wt %),^{1,5} the biomimetically grown surface layer of bioglasses constitutes a minor fraction out of the entire BG-dominated specimen, thereby compromising NMR signal sensitivity and complicating the investigations. More progress is required in this area to improve the structural understanding of the bioactive layer that interfaces the implant and the living organism.

By utilizing ^{29}Si and ^{31}P magic-angle spinning (MAS) NMR, we recently reported a study²⁸ of the reactions leading to HCA formation at the surface of an ordered mesoporous bioactive glass^{8,21–23} (MBG) of composition $10\text{CaO}-85\text{SiO}_2-5\text{P}_2\text{O}_5$ in a simulated body fluid (SBF).⁴³ Here, we examine the characteristics of the biomimetically grown ACP and HCA constituents of the surface layer generated either in SBF or buffered water media from a very similar MBG specimen, by using transmission electron microscopy (TEM), and particularly ^{31}P and ^1H MAS NMR. We contrast the $^1\text{H} \rightarrow ^{31}\text{P}$ cross-polarization (CP) dynamics observed

Received: July 1, 2011

Revised: September 8, 2011

Published: September 09, 2011

from the amorphous and structurally ordered components of the phosphate layer with that of a synthetic crystalline hydroxyapatite sample (labeled “HAref”) as well as with the *amorphous calcium phosphate* clusters (henceforth referred to as “CaP”) initially present in the MBG pore wall.^{28,44,45} Such experimentation provides qualitative information about the (shortest) ^1H – ^{31}P internuclear distances in a structure, here revealing very similar ^1H – ^{31}P spatial contacts in each pair of amorphous CaP/ACP and crystalline HCA/HAref phases: this underscores the close structural similarity between the orthophosphate component of the MBG structure^{28,44,45} and the biomimetic ACP formed in vitro, on one hand, and the biomimetic apatite compared with the crystalline reference, on the other.

2. MATERIALS AND METHODS

2.1. Mesoporous Bioactive Glass Preparation and in Vitro Studies. An MBG sample of nominal molar composition 10CaO – 85SiO_2 – $5\text{P}_2\text{O}_5$, onward labeled “S85” according to its mol % of SiO_2 , was prepared at 40°C using an evaporation-induced self-assembly (EISA) process⁴⁶ with the P123 triblock copolymer as structure-directing agent, as described in ref 23. Tetraethyl orthosilicate (TEOS), triethyl phosphate (TEP), and $\text{Ca}(\text{NO}_3)_2 \cdot 4\text{H}_2\text{O}$ served as precursors for introducing each of the elements Si, P, and Ca, respectively. The reaction produced homogeneous membranes that were calcined at 700°C for 6 h to remove organic species and nitrate ions. X-ray fluorescence (XRF) spectroscopy employing a Philips PANalytical AXIOS spectrometer (Philips Electronics NV) and X-rays generated by the Rh K_α line at $\lambda = 0.614 \text{ \AA}$ yielded a charge-balanced analyzed composition of $\text{Ca}_{0.098}\text{Si}_{0.838}\text{P}_{0.064}\text{O}_{1.93}$.

An SBF solution was prepared according to Kokubo et al.⁴³ by dissolving NaCl, KCl, NaHCO_3 , $\text{K}_2\text{HPO}_4 \cdot 3\text{H}_2\text{O}$, $\text{MgCl}_2 \cdot 6\text{H}_2\text{O}$, CaCl_2 , and Na_2SO_4 in distilled water. The solution was buffered at pH 7.45 by using tris(hydroxymethyl)-aminomethane/HCl (“TRIS”) and passed through a $0.22 \mu\text{m}$ Millipore filter to avoid bacterial contamination. Additionally, the in vitro studies involved a medium of distilled water, buffered by TRIS/HCl to provide the same pH value as the SBF. These two distinct solutions are henceforth denoted “SBF” and “TRIS”, respectively.

The in vitro apatite formation was investigated by immersing 1.00 g of S85 grains in 50 mL of either SBF or TRIS solutions for 16 h: the resulting specimens are henceforth referred to as “*sbfl6h*” and “*tris16h*” respectively. The SBF/TRIS-soaking was performed at 37°C , employing a sealed polyethylene container under continuous orbital stirring (100 rpm) in an Ecotron HT incubator. Each sample was filtered and washed with water to quench the surface reactions and removing potentially precipitated salts. It was subsequently vacuum-dried at 37°C for several days.

2.2. Transmission Electron Microscopy. Finely ground specimens were sprinkled on a carbon film with holes, supported by a copper grid. They were examined in a field-emission gun transmission electron microscope (JEM 2100F; JEOL, Japan) at 200 kV acceleration voltage. TEM images were recorded with a CCD camera (Ultra Scan) from Gatan. Cation compositions were determined on selected fragments by EDX, employing a retractable detector with an ultrathin window, and using the JEOL JED-2300 software for data analysis.

2.3. Solid-State Nuclear Magnetic Resonance. All NMR experimentation employed finely ground samples filled in 6 mm zirconia pencil rotors undergoing MAS at 9.0 kHz. An Agilent/Varian/Chemagnetics Infinity 400 spectrometer was utilized at a magnetic field of 9.4 T, giving Larmor frequencies of -162.0 MHz

for ^{31}P and -400.1 MHz for ^1H in the frequency-sign convention recommended by Levitt.⁴⁷

Single-pulse (“Bloch-decay”) ^{31}P NMR experiments employed $\approx 70^\circ$ flip-angles at a nutation frequency of $\omega_{\text{nuc}}^{\text{P}}/2\pi = 48 \text{ kHz}$. Typically, ≈ 340 signal transients (36 transients for HAref) were coadded, using relaxation delays of 600 s. ^1H NMR spectra were recorded by Hahn spin–echoes⁴⁸ by employing $\omega_{\text{nuc}}^{\text{H}}/2\pi = 48 \text{ kHz}$ (used for “hard” ^1H pulses throughout all experimentation), an echo delay of $\tau_{\text{echo}} = 111 \mu\text{s}$, 5.0 s of relaxation delay, and 1024 transients/acquisition. Ramped⁴⁹ ^1H → ^{31}P CP^{48,50,51} was established at the modified Hartmann–Hahn condition $\omega_{\text{nuc}}^{\text{H}} - \omega_{\text{nuc}}^{\text{P}} = 2\omega_r$, giving nutation frequencies of 20 and 38 kHz for ^{31}P and ^1H , respectively, at the spinning frequency $\omega_r/2\pi = 9.0 \text{ kHz}$. Between 4096 and 14 336 transients were accumulated for variable contact intervals (τ_{CP}), using relaxation delays of 4.0 s.

^1H – ^{31}P heteronuclear correlation (HETCOR) 2D NMR spectra were acquired from the S85, *sbfl6h*, and *tris16h* specimens using ^1H → ^{31}P CP for magnetization transfer ($\tau_{\text{CP}} = 1.5 \text{ ms}$) and ≈ 800 accumulated signal transients/ t_1 -value (except for S85: 1616 transients/ t_1). The spectral window was 22 kHz both for the direct (^{31}P ; horizontal) and indirect (^1H ; vertical) spectral dimensions, respectively, except for *sbfl6h* (16 kHz for the ^1H dimension). Time-proportional phase incrementation⁴⁸ arranged absorptive 2D NMR spectra with frequency sign discrimination along the indirect dimension, thereby reducing its effective range by 1/2. We acquired $110(t_1) \times 250(t_2)$ data points, which were zero-filled to a (256×1024) grid before 2D Fourier transformation. Other experimental parameters were identical to those of the 1D CPMAS acquisitions.

We verified that the application of high-power ^1H decoupling did not affect the ^{31}P NMR peak widths perceptibly, and all experimentation was performed without ^1H decoupling, including the NMR relaxation measurements discussed in Section 3.5. The processing of the 1D NMR spectra did not involve signal apodization, whereas for the 2D HETCOR data set, 80 Hz Gaussian and 20 Hz (40 Hz for S85) Lorentzian broadening was applied along the ^{31}P and ^1H dimensions, respectively. Chemical shifts are quoted relative to 85% H_3PO_4 (^{31}P) and neat tetramethylsilane (^1H).

3. RESULTS

3.1. Transmission Electron Microscopy. High-resolution TEM was employed to investigate the nanostructure and composition of the S85 MBG before and after its soaking in SBF and TRIS solutions. Figure 1a shows an image recorded from pristine S85. Electron diffraction (ED) verified an amorphous material, whereas elemental compositions probed by EDX measurements at selected spots accorded very well with that of the XRF analysis.

Representative TEM images recorded from fragments of the *sbfl6h* and *tris16h* specimens are displayed in Figure 1b and 1c, respectively: they evidence a large number of 10–50 nm sized elongated particles grown at the MBG surface. Their crystalline character is evident from both the TEM image shown in Figure 1d that reveals needle-shaped nanocrystals and the accompanying ED pattern (inset). Cation compositions probed by TEM/EDX over a collection of fragments from the *sbfl6h* and *tris16h* specimens revealed $n_{\text{Ca}}/n_{\text{P}}$ molar ratios scattered around the HA characteristic value of 1.7. Results from both powder X-ray diffraction and scanning electron microscopy (SEM) coupled to EDX further confirmed the presence of HA in the MBG surface layer.²⁹

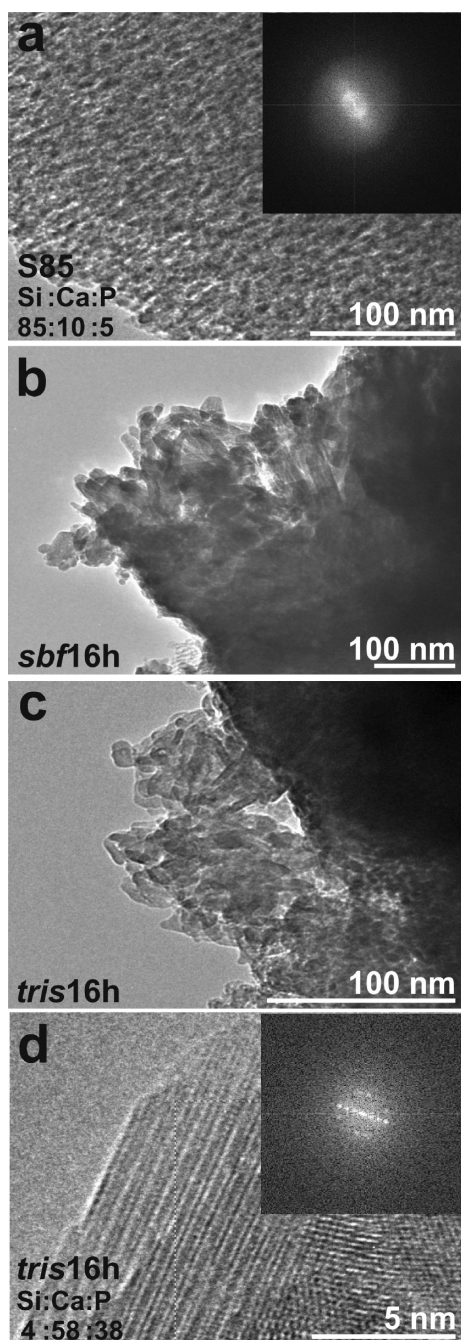


Figure 1. TEM images recorded from fragments of the (a) pristine S85, (b) *sbf16h*, and (c,d) *tris16h* specimens, with accompanying ED patterns displayed as insets in image a and d. The dark areas in panels b and c correspond to the Si-rich MBG, whereas lighter domains represent the phosphate layer. (d) Zoom of the image in c, revealing an elongated HA crystal. Cation compositions measured by EDX over the displayed areas are reported in at % at the bottom left corner of the images a and d.

Onward, we will employ the label “H(C)A” when referring collectively to the biomimetic apatite phase forming in either SBF or TRIS solutions: note that ACP crystallizes into HA in TRIS/HCl-buffered water, whereas the presence of carbonate ions in the SBF solution⁴³ leads to the formation of HCA, analogously to bone and tooth formed in vivo.^{6–8} The simultaneous incorporation of

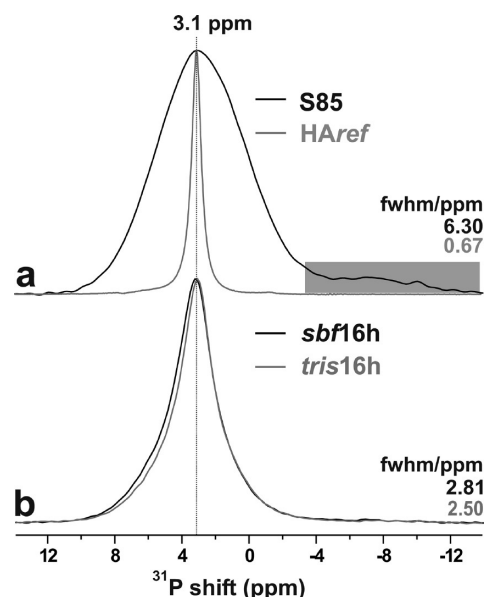


Figure 2. ^{31}P MAS NMR spectra acquired by single pulses from the (a) pristine S85 (black trace) and crystalline HAref (gray line) samples. The gray rectangle in panel a marks a minor resonance assigned to P–O–Si moieties.^{28,44} (b) After MBG exposure to SBF (black trace) or TRIS (gray trace) solutions for 16 h.

Na^+ and CO_3^{2-} ions into the SBF-induced calcium phosphate layer at the S85 surface was recently evidenced by SEM/EDX,²⁹ ^{23}Na MAS, and ^{13}C CPMAS NMR.²⁸

3.2. Single-Pulse ^{31}P NMR Spectra. Figure 2 shows ^{31}P MAS NMR spectra acquired directly by single pulses that quantitatively reflect the various P populations of each sample, as opposed to those recorded by $^1\text{H} \rightarrow ^{31}\text{P}$ CP (discussed below) that draw their magnetization from neighboring ^1H species, thereby emphasizing ^{31}P sites in close proximity to protons. Figure 2a displays the results from the pristine S85 MBG sample and the crystalline hydroxyapatite reference specimen, “HAref”. The Ca^{2+} and PO_4^{3-} ions within/at the $\text{CaO-SiO}_2\text{-P}_2\text{O}_5$ MBG pore wall form nanometer-sized CaP clusters.^{28,44,45} Hence, accompanying their common orthophosphate structural building blocks, both HAref and the CaP component of S85 produce a ^{31}P NMR peak maximum around 3 ppm. However, the very different ordering of the two structures is reflected by their distinct peak shapes and full width at half-maximum (fwhm) height of the corresponding ^{31}P NMR signals: the NMR response from the well-ordered HAref structure features a narrow Lorentzian peak (0.67 ppm), whereas that from the MBG is Gaussian-shaped and an order of magnitude broader (6.3 ppm). As previously highlighted^{28,44} and explored further in this contribution, the CaP clusters of S85 share many NMR— and hence local structural—features with the ACP layer initially forming at the MBG surface on its contact with (simulated) body fluids.

Figure 2b displays the ^{31}P NMR spectra resulting after soaking the S85 MBG for 16 h in either TRIS/HCl or SBF solutions. Both reveal a significant signal-narrowing and the presence of two ^{31}P sources in the specimens, reflecting one ordered phase (i.e., biomimetic H(C)A) and two amorphous components, that is, CaP and ACP. The latter cannot readily be distinguished by their 1D NMR-associated parameters; however, as the surface-associated CaP clusters tend to rapidly dissolve during the initial stages of the MBG soaking, their contributions to the ^{31}P NMR spectra of the *sbf16h* and *tris16h* samples are expected to be minor.

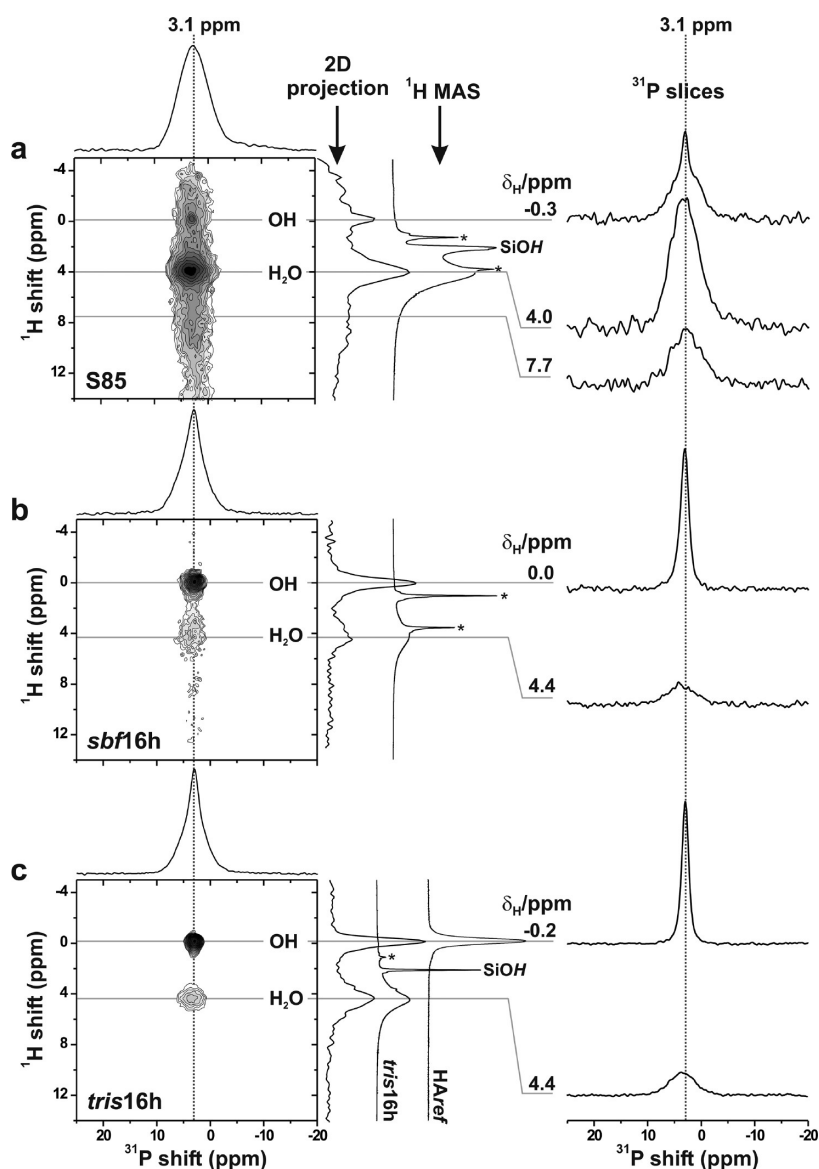


Figure 3. Left panel: ^1H - ^{31}P 2D HETCOR NMR spectra recorded from the (a) S85, (b) *sbf16h*, and (c) *tris16h* specimens. They are shown together with sum projections along each spectral dimension, as well as directly excited ^1H MAS NMR spectra (mid-panel). The latter reveal a primary resonance around 4 ppm from water molecules, a narrow peak at 2.1 ppm from “isolated” silanols (labeled “SiOH”), and signals from minor remainings of organic templating moieties (marked by asterisks). In c, the ^1H MAS NMR spectrum of HAref is also displayed. Right panel: Slices along the as-indicated ^1H chemical shifts around 0 (top trace) and 4 ppm (bottom trace) of each 2D spectrum: they either comprise a narrow (top) or broad (bottom) ^{31}P NMR peak, stemming from biomimetic H(C)A and amorphous ACP/CaP components, respectively.

These peak assignments were motivated further by Gunawidjaja et al.²⁸ Spectral deconvolution results (discussed in detail elsewhere²⁹) yielded very close values of the chemical shift ($\delta \approx 3.5$ ppm) and peak widths (fwhm ≈ 5.4 ppm) for biomimetic ACP in both *sbf16h* and *tris16h* specimens, whereas the corresponding parameters for H(C)A were as follows: $\delta = 3.18$ ppm, fwhm = 1.94 ppm for *sbf16h*; $\delta = 3.08$ ppm, fwhm = 1.80 ppm for *tris16h*. The relative amounts of apatite out of all P-bearing phases were estimated to be 43 % and 50% for the *sbf16h* and *tris16h* specimens, respectively.

3.3. ^1H - ^{31}P 2D HETCOR NMR. The identifications of broad and narrow ^{31}P NMR signal portions in Figure 2b to indeed stem from amorphous CaP/ACP and H(C)A phases are proven by the ^1H - ^{31}P HETCOR 2D NMR spectra of Figure 3, which were recorded from the (a) S85, (b) *sbf16h*, and (c) *tris16h* specimens.

This experiment incorporates $^1\text{H} \rightarrow ^{31}\text{P}$ CP for magnetization transfers (as discussed in Section 3.4); an NMR peak appearing at the 2D shift-coordinate (δ_{H} , δ_{P}) evidences a close spatial proximity between the ^1H and ^{31}P sites associated with each respective chemical shift.⁴⁸ The left panel of Figure 3 shows the 2D NMR spectra as well as their projections along the ^{31}P (horizontal) and ^1H (vertical) dimensions. The mid panel comprises directly excited ^1H MAS NMR spectra. Because each of the latter *quantitatively* reflects all ^1H environments of the sample, a comparison with its respective HETCOR projection reveals *which* proton sites are associated with *which* respective phosphate- and silicate-bearing MBG components, respectively. This is most transparently appreciated from Figure 4 that displays the ^1H MAS spectra and HETCOR projections in a larger format.

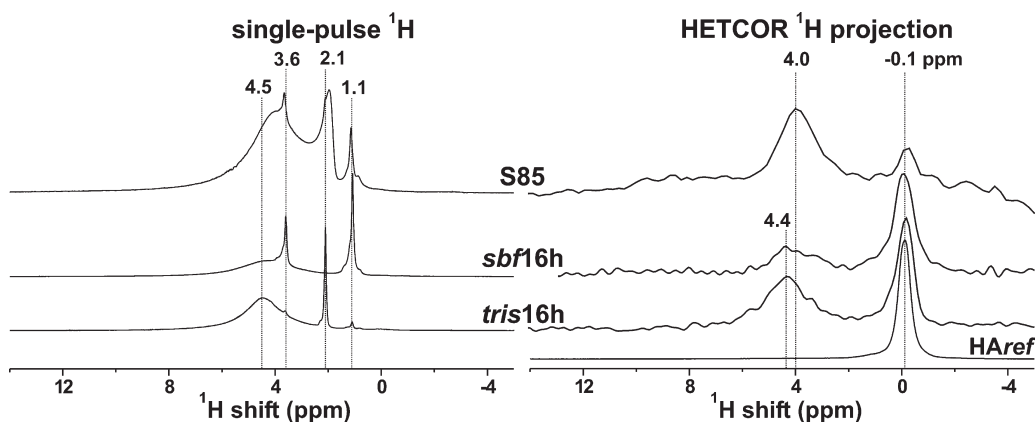


Figure 4. Directly excited ^1H MAS NMR spectra (left panel) and projections along the ^1H dimension of 2D HETCOR spectra (right panel). For comparison, the directly excited ^1H spectrum from HAref is also displayed at the bottom of the right panel.

The present HETCOR 2D NMR spectra appear similar to our previously presented results from analogous pristine⁴⁴ and SBF-treated²⁸ S85 samples. Each amorphous (ACP/CaP) and crystalline (H(C)A) phosphate phase is primarily associated with proton environments stemming from water molecules and hydroxyl groups, respectively, which resonates at $\delta_{\text{H}} \approx 4$ ppm (broad peak) and ≈ 0 ppm (narrow signal), respectively.^{28,44} The latter shift is a fingerprint of hydroxyapatite, cf. the ^1H MAS NMR spectrum from HAref shown in Figure 4. Because of the very low amount of such phosphate-associated OH moieties relative to the entire proton ensemble in the S85-deriving specimens, the accompanying signal $\delta_{\text{H}} \approx 0$ is visible solely in the HETCOR projections, whereas it remains undetectable in directly excited ^1H NMR spectra (Figure 4). The dual presence of amorphous and crystalline phosphates in the SBF/TRIS-exposed samples is unambiguously evidenced from the 2D NMR spectra of Figure 3b,c that primarily reveal two NMR correlations, centered at the pairs of shifts $\{\delta_{\text{H}}, \delta_{\text{P}}\}$ around $\{4, 3\}$ ppm and $\{0, 3\}$ ppm: each respective slice along the ^{31}P spectral dimension (right panel) comprises one broad and one narrow ^{31}P NMR peak, as indeed suggested by the 1D ^{31}P NMR spectra of Figure 2.

Given these observations, it is noteworthy that the broad ^{31}P NMR signal from the CaP clusters of the pristine S85 MBG correlates with those of *both* the ^1H resonances from water molecules and the OH groups. This proves that whereas the structural properties of the CaP clusters are predominantly shared by those of ACP, they exhibit some features associated with HA, such as the presence of minor amounts of its characteristic hydroxy groups. Previously, we suggested the presence of such OH moieties in the CaP clusters of MBGs, observed tentatively from a 2D HETCOR spectrum of an S85 sample associated with a composition close to the current one;⁴⁴ however, this ^1H NMR signal is sufficiently resolved in the present HETCOR 2D spectrum to eliminate any ambiguity. Furthermore, it is interesting that the slice along the ^{31}P dimension taken at $\delta_{\text{H}} = 0$ (Figure 3a; right panel) hints *two distinct* ^{31}P NMR signals: one broad and one narrow. The latter indicates a local ordering in a minor population of the phosphate/hydroxyl groups of the CaP clusters, presumably induced by the calcination process. (See Section 2.1.)

Whereas the ^1H dimension of the HETCOR spectrum from S85 is very broad, a weak NMR signal is discernible in the δ_{H} region around 8–10 ppm, which may signify minor amounts of acidic P–O ^1H moieties associated with the CaP clusters. Yet, the 2D HETCOR NMR spectra in Figure 3, particularly those from

sbf16h and *tris16h*, reveal that if present, the population of such acidic protons must be very low.

All other resonances present in the directly excited ^1H NMR spectra shown in the left panel of Figure 4 were assigned and discussed by Leonova et al.⁴⁴ This includes the sharp peak at 2.1 ppm arising from “isolated” (non-hydrogen-bonded) silanols at the silica surface as well as those from minute remainings of organic precursor/templating molecules that appear at 3.6 ppm and 1.1 ppm in the NMR spectra.

3.4. $^1\text{H} \rightarrow ^{31}\text{P}$ CP Dynamics. A $^1\text{H} \rightarrow ^{31}\text{P}$ CPMAS experiment excites ^{31}P NMR signals by transferring magnetization from nearby protons at a rate that depends exponentially on T_{CP}^{-1} : for an “isolated” $^1\text{H} - ^{31}\text{P}$ spin-pair, this CP time constant (T_{CP}) is proportional to the inverse square of the heteronuclear through-space dipolar coupling constant b , that is, to the sixth power of the $^1\text{H} - ^{31}\text{P}$ internuclear distance r : $T_{\text{CP}} \sim b^{-2} \sim r^6$.^{48,50,51} The efficiency of the magnetization transfer, that is, the observed ^{31}P NMR signal strength, is dictated by the ratio $\tau_{\text{CP}}/T_{\text{CP}}$, where the contact interval τ_{CP} represents the duration of the CP process. Hence, by employing small τ_{CP} values, one may experimentally arrange the sole excitation of NMR signals from the ^{31}P sites being in close spatial proximity to protons (within a few angstroms), whereas prolonged CPMAS application will effect long-range $^1\text{H} \rightarrow ^{31}\text{P}$ magnetization transfers.

However, in relatively dense structures, such as the calcium phosphates of the present work, a multitude of distinct through-space $^1\text{H} - ^{31}\text{P}$ dipolar interactions will contribute to the observed CP dynamics. Whereas T_{CP} is extractable as a phenomenological parameter by variable- τ_{CP} CPMAS experimentation,^{50,51} it may only be interpreted in terms of an *effective* dipolar coupling constant, b_{eff} , associated with an internuclear distance, r_{eff} . Yet, the CP kinetics is dominated by the set of *largest* coupling constants of each ^{31}P site, that is, those involving the shortest $^1\text{H} - ^{31}\text{P}$ distances. When these distinct b values display nearly equal sizes, $|b_{jk}| \approx |b_{jm}| \approx \dots$ (where each subscript denotes the spin-pair index), their contributions are roughly additive^{50–52}

$$T_{\text{CP}}^{-1} \sim b_{\text{eff}}^2 \approx \sum_{jk}^{\text{all pairs}} b_{jk}^2. \quad (1)$$

Herein, we will use the terminology of strong (or weak) $^1\text{H} - ^{31}\text{P}$ contact when referring to a short (long) effective internuclear distance, which is associated with a low (high) T_{CP} -value.

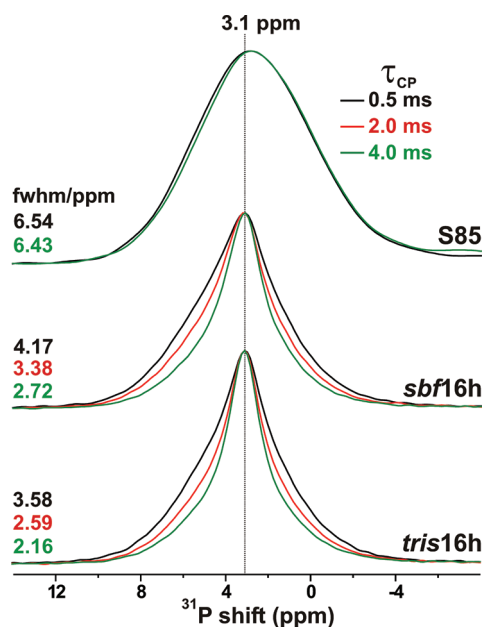


Figure 5. $^1\text{H} \rightarrow ^{31}\text{P}$ CPMAS NMR spectra acquired from the as-indicated samples (see right spectral portion) using three distinct CP contact intervals according to 0.5 ms (black), 2.0 ms (red), and 4.0 ms (green). The full width at half-maximum (fwhm; in ppm) height of each ^{31}P peak is specified at the left bottom part of each spectrum.

Figure 5 conveys the dependence of the ^{31}P NMR peakshapes acquired by using three distinct $^1\text{H} \rightarrow ^{31}\text{P}$ CP contact intervals for each MBG specimen. Note that the NMR signals from the ^{31}P sites in closest proximity to protons are emphasized in CPMAS acquisitions employing the shortest value $\tau_{\text{CP}} = 0.5$ ms. As opposed to the spectra of Figure 2, which quantitatively reveal the various phosphate populations, the peakshape alterations in Figure 5 for variable τ_{CP} values suggest distinct $^1\text{H} - ^{31}\text{P}$ contacts in the different phosphate-bearing phases present in the SBF/TRIS-soaked S85 samples. Striking differences are observed when τ_{CP} is varied for each of the *sbf16h* and *tris16h* specimens: the shortest contact interval $\tau_{\text{CP}} = 0.5$ ms emphasizes the broad NMR signal from ACP relative to its crystalline counterpart. The contribution from the latter grows for increasing τ_{CP} values, which accounts for the concomitant narrowing of the net ^{31}P NMR peak. The most likely reason for this observation is enhanced $^1\text{H} - ^{31}\text{P}$ contacts stemming from a larger total proton content in the ACP/CaP phases (compared with that in the more ordered H(C)A structure), whereas the respective shortest inter-nuclear distance is comparable within all structures.

On the other hand, the absence of line shape alterations observed from the pristine S85 MBG throughout the entire range of τ_{CP} values evidences uniform $^{31}\text{P} - ^1\text{H}$ contacts in the CaP clusters of its pore walls. Furthermore, these NMR spectra (Figure 5) are also essentially identical to that obtained by single pulses in Figure 2a. These observations for the amorphous CaP clusters mirror analogous reports by single-pulse and CPMAS ^{31}P NMR on synthetic ACP.^{53–55}

To gain more quantitative insight into the CP dynamics and $^1\text{H} - ^{31}\text{P}$ contacts in the various phosphorus-bearing phases grown from the S85-surface, we conducted a larger series of CPMAS NMR experiments with variable τ_{CP} values for the S85, *tris16h*, and *HAref* samples. Because of their single-phase character, integration of each ^{31}P peak from the *HAref* and S85

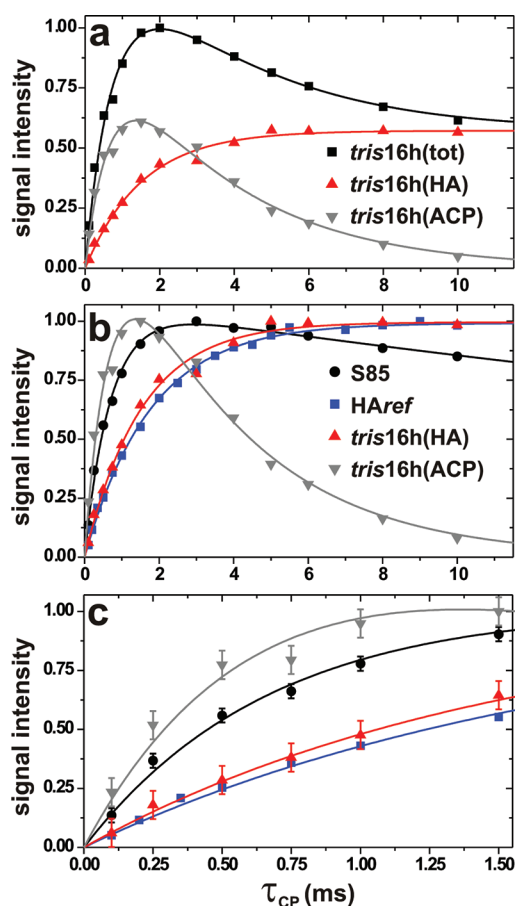


Figure 6. Integrated $^1\text{H} \rightarrow ^{31}\text{P}$ CPMAS NMR-signal intensities plotted for variable contact intervals (τ_{CP}) and shown together with best fits to eqs 4 or 5. (a) Results obtained from the *tris16h* sample. The total signal buildup (“tot”; black symbols) is shown together with its respective amorphous (“ACP”; gray symbols) and crystalline (“HA”; red) components. (b) Integrated signal intensities and best-fit curves obtained from the as-indicated samples of S85, *HAref*, and the *tris16h*(ACP) and *tris16h*(HA) components displayed in panel a. For facilitating comparison, each signal buildup curve is normalized to the same maximum amplitude. (c) Zoom of diagram b over $0 \leq \tau_{\text{CP}} \leq 1.55$ ms, emphasizing the distinct initial rates of the magnetization transfers. To improve visualization, the experimental uncertainties are indicated only in diagram c.

specimens provided directly the NMR signal-buildup representative for the ^{31}P sites of each respective crystalline and amorphous component. For *tris16h*, on the other hand, its ^{31}P NMR peak required deconvolution into two signals stemming from the ACP and HA constituents, respectively. These results are plotted in Figure 6a, together with best-fit curves (discussed in Section 3.6) that reveal each of the ACP and HA contributions. As suggested from Figure 5, the HA phase indeed manifests a significantly slower ^{31}P NMR signal buildup compared with its amorphous counterparts.

Figures 6b,c compare the CP kinetics observed for the apatite ^{31}P environments in *HAref* and *tris16h* as well as the amorphous phosphates, CaP (of S85) and ACP (of *tris16h*). We conclude that both amorphous components display similar initial ^{31}P NMR signal buildup, which is faster than that observed from the two crystalline phases. The latter pair also exhibits essentially identical CP dynamics.

3.5. Estimated $T_{1\rho}$ Relaxation Time-Constants. Before analyzing the $^1\text{H} \rightarrow ^{31}\text{P}$ CP dynamics in detail, we inspect the associated relaxation (decay) processes of the transverse ^1H and

^{31}P magnetization in the presence of an applied rf field ($T_{1\rho}$) for each relevant $^1\text{H}_2\text{O}$ and O^1H resonance—as well as that of each $^{31}\text{PO}_4^{3-}$ site—of the amorphous and crystalline phosphate constituents of the S85, HAref, and tris16h specimens. The rate of magnetization decay is dictated by $T_{1\rho}^{-1}$, where the time-constant $T_{1\rho}$ depends on both the external magnetic field and the MAS frequency, but is primarily dictated by molecular motions over a time scale of the inverse rf nutation frequency ($\sim\omega_{\text{nut}}^{-1}$) that (for instance) may modulate heteronuclear dipolar interactions at the spin site to drive relaxation.^{36,48,51}

The NMR signal decays were probed by appending a spin-lock pulse^{36,48,51} of variable duration (τ_{SL}) either to the excitation pulse (for ^1H), or to the contact interval in a CP-based experiment (for ^{31}P). The nutation frequency of the spin-lock pulse was identical to that employed during CP for each respective ^1H and ^{31}P spin species, except for the absence of a ramped ^{31}P rf amplitude. Except for the apatite O^1H groups present in the tris16h sample, whose signal is not discernable in directly excited ^1H spectra (see Section 3.3), all proton relaxation time constants were obtained by direct integration of the well-resolved NMR peaks from O^1H groups in HAref and from the $^1\text{H}_2\text{O}$ molecules in S85 and tris16h. However, note that for the S85-deriving samples, the latter measurements reflect the *entire* water reservoir, which mainly derives from protons associated with the *silicate* portion of the MBG surface. To circumvent the slow ^{31}P spin–lattice (T_1) relaxation discussed in Section 4.3 (Table 2), the ^{31}P $T_{1\rho}$ values were estimated by numerically fitting the directly integrated $^{31}\text{PO}_4^{3-}$ NMR signals acquired by ^1H spin-locking followed by $^1\text{H}\rightarrow^{31}\text{P}$ CP. Utilizing CPMAS is advantageous because it ensures the sole probing of the ^1H and ^{31}P sites present in the *phosphate* phases. However, the analysis of some of these experiments (as well as in Section 3.6) relies on exclusive magnetization transfers within the following ^1H and ^{31}P pairs: $^1\text{H}_2\text{O}\leftrightarrow^{31}\text{PO}_4^{3-}$ (amorphous) and $\text{O}^1\text{H}\leftrightarrow^{31}\text{PO}_4^{3-}$ (crystalline); this assumption is justified by the 2D HETCOR NMR results in Figure 3 (see Section 3.3).

The results of the NMR relaxation measurements are plotted in Figure 7. The integrated peak intensities, $I(\tau_{\text{SL}})$, were fit to the following expressions that involve either one (eq 2) or two (A and B; eq 3) components^{36,48}

$$I_X(\tau_{\text{SL}}) = I_0 \exp\{-\tau_{\text{SL}}/T_{1\rho}^X\}, \quad X = \text{H or P}, \quad (2)$$

$$I_X(\tau_{\text{SL}}) = I_0[x_A \exp\{-\tau_{\text{SL}}/T_{1\rho}^{X,A}\} + x_B \exp\{-\tau_{\text{SL}}/T_{1\rho}^{X,B}\}], \quad X = \text{H or P}, \quad (3)$$

where I_0 is proportional to the ^1H or ^{31}P population, and $T_{1\rho}^{\text{H}}$ and $T_{1\rho}^{\text{P}}$ represent the respective ^1H and ^{31}P relaxation time constants. For the cases of biexponential decays in eq 3, the signal fractions $\{x_A, x_B\}$ associated with the respective parameters $\{T_{1\rho}^{X,A}, T_{1\rho}^{X,B}\}$ obey $x_A + x_B = 1$. Biexponential decays were generally observed for both ^1H and ^{31}P when τ_{SL} increased (Figure 7), except for the ACP component of tris16h [*“tris16h(ACP)”*]; its $^1\text{H}_2\text{O}$ magnetization displayed a monoexponential damping, whereas the orthophosphate signal-decay fitted equally well to eq 2, thereby giving the single parameter $T_{1\rho}^{\text{P}} = 4.74$ ms ($R^2 = 0.989$).

The resulting time constants $\{T_{1\rho}^{X,A}, T_{1\rho}^{X,B}\}$ and weights $\{x_A, x_B\}$ are given in Table 2, with the component displaying the largest fraction listed topmost. In general, we obtained a pair involving one rapidly (low $T_{1\rho}$ value) and one slowly (large $T_{1\rho}$) relaxing component. Because CP invariably underestimates the contributions

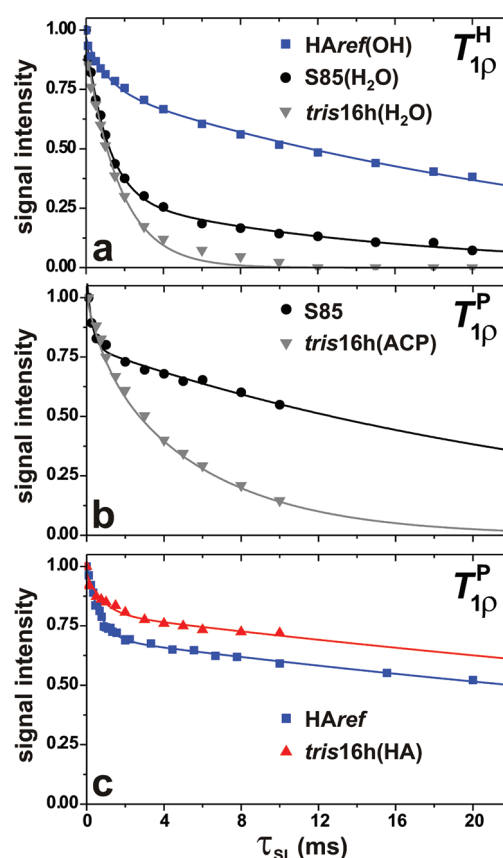


Figure 7. Transverse magnetization-decay of (a) ^1H and (b,c) ^{31}P due to relaxation during spin-locking by an rf field, plotted for variable spin-lock intervals (τ_{SL}) and the integrated NMR signals of the following nuclei (indicated by bold letters): (a) O^1H of HAref and $^1\text{H}_2\text{O}$ in S85 and tris16h, respectively; (b) $^{31}\text{PO}_4^{3-}$ groups in the CaP clusters of pristine S85, and the ACP phase of tris16h; and (c) $^{31}\text{PO}_4^{3-}$ of HAref and the HA component of tris16h.

from rapidly decaying signals, the relative populations accounting for the biexponential decays of the ^{31}P sites may only be interpreted semiquantitatively. The biexponential relaxation observed for the two S85-deriving specimens is not surprising, given their complex multicomponent character, whereas for the case of HAref, they may stem from hydroxy and phosphate ions present at the surface and interior of the crystallites, respectively, as discussed by Isobe et al.⁵⁶ and Jäger et al.⁵⁷ in the context of nanocrystalline HA.

3.6. Cross Polarization Kinetics Parameters. To determine both the underlying time constant (T_{CP}) and damping parameters ($T_{1\rho}^{\text{H}}, T_{1\rho}^{\text{P}}$) of each CP buildup curve in Figure 6, we fitted the integrated signal intensity of each NMR peak, $I(\tau_{\text{CP}})$, to either of the following expressions^{50,51}

$$I(\tau_{\text{CP}}) = I_0[1 - \exp\{-\tau_{\text{CP}}/T_{\text{CP}}\}] \quad (4)$$

$$I(\tau_{\text{CP}}) = I_0(1 - T_{\text{CP}}/T_{1\rho}^{\text{H}})^{-1}[\exp\{-\tau_{\text{CP}}/T_{1\rho}^{\text{H}}\} - \exp\{-\tau_{\text{CP}}/T_{\text{CP}}\}] \quad (5)$$

$$I(\tau_{\text{CP}}; T_{1\rho}^{\text{P}}) = I_0(1 + T_{\text{CP}}/T_{1\rho}^{\text{P}} - T_{\text{CP}}/T_{1\rho}^{\text{H}})^{-1}[\exp\{-\tau_{\text{CP}}/T_{1\rho}^{\text{H}}\} - \exp\{-\tau_{\text{CP}}(1/T_{\text{CP}} + 1/T_{1\rho}^{\text{P}})\}], \text{ with } T_{1\rho}^{\text{P}} \text{ fixed.} \quad (6)$$

Equations 4–6 are valid when (i) $T_{CP} \ll (T_{1\rho}^H, T_{1\rho}^P)$ and assume (ii) the absence of spin-diffusion among protons and that (iii) the ^1H population grossly outnumbers that of ^{31}P .^{36,38,51} The first two requirements are generally met under our experimental conditions (a spinning rate of 9.0 kHz and low ^1H contents of the samples), but the third assumption is more questionable. Furthermore, to improve the NMR spectral signal-to-noise and the CP-transfer stability, all of our CPMAS experimentation involved ramping of the ^{31}P rf field,⁴⁹ which decelerates the magnetization transfers relative to traditional “constant amplitude” Hartmann–Hahn matching. For these reasons, we focus primarily on qualitatively comparing the CP kinetics and best-fit T_{CP} , $T_{1\rho}^H$, and $T_{1\rho}^P$ parameters among the three samples of the present study, which were all recorded under identical experimental conditions.

The (large) values of $T_{1\rho}^H$ and $T_{1\rho}^P$ from the *tris*16h(HA) and HAref components (see Table 2) were not possible to estimate within the range $\tau_{CP} \leq 10$ ms available to us to avoid compromising the integrity of our old MAS probehead; consequently, these data were fitted to eq 4. The directly measured ^{31}P NMR signal decays of the amorphous CaP and ACP constituents of the S85 and *tris*16h specimens reveal significantly damped curves (section 3.5). Hence, their CP kinetics data were fitted to both eqs 5 and 6 for the latter case assuming a single T_{CP} parameter and fixed value(s) of $T_{1\rho}^P$ as obtained from the independent fitting of each respective spin-lock decay, by using eq 2 for *tris*16h(ACP) and eq 3 for S85. The two damping constants $\{T_{1\rho}^{P,A}, T_{1\rho}^{P,B}\}$ and their accompanying fractions $\{x_A, x_B\}$ associated with S85 (from Table 2) were employed to fit the experimental data to the weighted sum $I(\tau_{CP}; T_{1\rho}^{P,A}, T_{1\rho}^{P,B}) = x_A I(\tau_{CP}; T_{1\rho}^{P,A}) + x_B I(\tau_{CP}; T_{1\rho}^{P,B})$, with each term evaluated from eq 6. Employing eq 6 with freely varying $T_{1\rho}^P$ values provided ill-defined “best-fit” parameters.

Table 3 lists the best-fit parameters. The T_{CP} values are indeed very similar for the two crystalline HA phases ($T_{CP} \geq 1.5$ ms) being roughly twice as large as those of the two amorphous CaP/ACP phosphates (0.69 ms to 0.80 ms). Besides differences in the CP rate constants, the primary distinction between the crystalline and amorphous P-bearing phases is their NMR relaxation in the presence of rf fields: both the CaP (of pristine S85) and ACP (of *tris*16h) phases display significantly faster NMR signal decays through their much smaller values of $T_{1\rho}^H$ and $T_{1\rho}^P$. Table 3 evidences very similar best-fit T_{CP} -values extracted from either eq 5 or 6, that is, regardless if the $T_{1\rho}^P$ relaxation was explicitly accounted for.

4. DISCUSSION

4.1. NMR Characteristics of Synthetic and Biomimetic HA.

The ^{31}P sites of the S85 structure display closest internuclear distances to water molecules (Figure 3). The most evident ^1H – ^{31}P contact in the SBF/TRIS-exposed samples is that from the biomimetic apatite-like phase, which becomes emphasized because of its very narrow ^1H resonance. Yet, its associated ^1H and ^{31}P NMR peak widths from the O^1H and $^{31}\text{PO}_4^{3-}$ environments of the SBF/TRIS exposed samples are significantly larger than those of the well-ordered HAref sample (see Table 1): the ^{31}P fwhm from the latter is 0.67 ppm, whereas the *tris*16h and *sb*16h counterparts amount to 2.50 ppm and 2.81 ppm, respectively. Their HETCOR-observed ^1H signals are also relatively broad, revealing fwhm values around 0.8 ppm (*tris*16h) and 1.2 ppm (*sb*16h), which may be contrasted with that of 0.5 ppm observed from HAref. This confirms a lower structural order of both the OH and PO_4^{3-} environments of the in-vitro-formed H(C)A phases.

Table 1. ^1H and ^{31}P NMR Parameters

sample	^{31}P single pulse ^a		2D HETCOR	
	δ_P^{max} (ppm)	fwhm (ppm)	$(\delta_H; \delta_P)[\text{HA}]^b$ (ppm)	fwhm[HA] (ppm) ^c
S85	3.06	6.30 ± 0.08	(−0.3; 3.1)	≈ 0.7 ; n.d.
<i>sb</i> 16h	3.22	2.81 ± 0.04	(0.0; 3.0)	1.2; 1.8
<i>tris</i> 16h	3.06	2.50 ± 0.04	(−0.15; 3.0)	0.8; 1.5
HAref	3.06	0.67 ± 0.02	n.d.	0.5 ^d

^a Peak maximum δ_P^{max} (whose uncertainty of ± 0.05 ppm is primarily dictated by the external chemical shift referencing) and full width at half-maximum (fwhm) of the ^{31}P peak obtained by direct excitation (Figure 2). ^b Chemical shift coordinates (δ_H, δ_P) at the center of gravity of the 2D NMR peak from the apatite environments (Figure 3). ^c fwhm of the ^1H and ^{31}P signals, respectively (separated by semicolon), obtained from the corresponding 2D slices in Figure 3. ^d fwhm of the O^1H peak observed by direct excitation.

Table 2. ^1H and ^{31}P NMR Relaxation Properties

sample/component	$T_{1\rho}^H$ (ms) ^{a,b}	$T_{1\rho}^P$ (ms) ^{a,c}	T_1 (s) ^d
HAref	28 ± 2 (0.79)	66 ± 4 (0.70)	8.8 ± 0.6
	1.1 ± 0.2 (0.21)	0.65 ± 0.04 (0.30)	
<i>tris</i> 16h(HA/OH) ^e	n.d.	80 ± 30 (0.83)	79 ± 1
		0.83 ± 0.3 (0.17)	
<i>tris</i> 16h(ACP/H ₂ O) ^f	1.8 ± 0.1	5.9 ± 0.3 (0.78)	79 ± 1
		0.96 ± 0.2 (0.22)	
S85	1.1 ± 0.1 (0.69)	27 ± 3 (0.73)	128 ± 4
	15 ± 2 (0.31)	0.28 ± 0.07 (0.27)	

^a Best-fit time constants (using either eq 2 or eq 3) for ^1H ($T_{1\rho}^H$) and ^{31}P ($T_{1\rho}^P$) responsible for the decay of transverse magnetization during a spin-lock rf field. The relative weight of each contribution to the biexponential decay is given within parentheses. ^b Measured using a 90° pulse, followed by a spin-lock pulse. ^c Measured using ^1H – ^{31}P CP ($\tau_{CP} = 1.5$ ms), followed by a spin-lock pulse. ^d Determined from a saturation-recovery experiment. Note that for the case of *tris*16h, only the T_1 -value representative for the *net* ^{31}P peak was measured. ^e Concerns the ordered apatite-like component giving the $\text{O}^1\text{H} \leftrightarrow ^{31}\text{PO}_4^{3-}$ correlation established by 2D HETCOR. ^f Concerns the ACP component responsible for the $^1\text{H}_2\text{O} \leftrightarrow ^{31}\text{PO}_4^{3-}$ correlation.

Note that the slightly narrower ^{31}P NMR signal observed in the single-pulse acquisitions (Figure 2) from the *tris*16h sample compared with its SBF-soaked counterpart is unambiguously established from the HETCOR slices (Figure 3b,c; right panel) that separate the ^{31}P resonance of the apatite phase from the others. Hence, whereas the signal narrowing in Figure 2 is primarily attributed to a larger H(C)A contribution out of the total amount of P-bearing phases in the *tris*16h specimen relative to its *sb*16h counterpart (as discussed in detail elsewhere for a larger set of samples²⁹), Table 2 evidences an inherently narrower ^{31}P signal from H(C)A grown in TRIS solution compared with SBF. This is attributed to an overall higher ordering of the former HA phase, stemming partially from its absence of CO_3^{2-} , Na^+ , and other substituted ions, as compared with the HCA structure generated from SBF.²⁸

4.2. Phosphorus-Proton Environments in ACP and HA.

Relatively few NMR properties are reported from synthetic^{44,53–55,58,59} or biomimetic^{25,28,29} ACP. The present investigation involves to our knowledge the first detailed account of the ^1H and ^{31}P NMR relaxation properties and CP time

Table 3. Best-Fit Parameters from Variable- τ_{CP} $^1\text{H} \rightarrow ^{31}\text{P}$ CP Experiments

sample/component	T_{CP} (ms)	$T_{1\rho}^{\text{H}}$ (ms)	I_0 (a.u.)	R^2
HAref ^a	1.77 ± 0.04	n.d.	0.99 ± 0.01	0.998
tris16h(HA/OH) ^{a,b}	1.52 ± 0.08	n.d.	1.00 ± 0.02	0.993
tris16h(ACP/H ₂ O) ^{c,d}	0.69 ± 0.09 (0.80 ± 0.12)	3.3 ± 0.4 (3.3 ± 0.4)	1.62 ± 0.12 (1.89 ± 0.17)	0.976 (0.976)
S85 ^d	0.69 ± 0.03 (0.80 ± 0.03)	45 ± 8 (40 ± 8)	1.05 ± 0.02 (1.37 ± 0.03)	0.994 (0.996)

^a Best-fit $\{T_{\text{CP}}, T_{1\rho}^{\text{H}}, T_{1\rho}^{\text{P}}\}$ results and correlation coefficients R^2 obtained by fitting the experimental integrated signal intensity to eq 4. ^b Concerns the ordered apatite-like component giving the $\text{O}^1\text{H} \leftrightarrow ^{31}\text{PO}_4^{3-}$ correlation established by 2D HETCOR. ^c Concerns the ACP component responsible for the $^1\text{H}_2\text{O} \leftrightarrow ^{31}\text{PO}_4^{3-}$ correlation. ^d Obtained by fitting experimental data to eq 5. Values within parentheses were obtained by instead employing eq 6 and the fixed value $T_{1\rho}^{\text{P}} = 4.74$ ms [for tris16h(ACP)], whereas for S85, the biexponential parameters $\{T_{1\rho}^{\text{X,A}} = 27, T_{1\rho}^{\text{X,B}} = 0.28\}$ ms and signal fractions $\{x_{\text{A}} = 0.73, x_{\text{B}} = 0.27\}$ were used from Table 2.

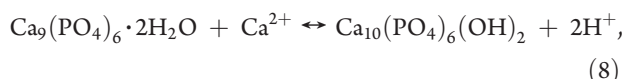
constants associated with two such phases: biomimetically grown ACP and the CaP clusters of MBGs. As unambiguously established by the $^1\text{H}-^{31}\text{P}$ HETCOR 2D NMR spectra in Figure 3b,c, the $^{31}\text{PO}_4^{3-}$ groups are in close spatial proximity solely to water molecules but neither to OH groups nor acidic protons, regardless if ACP is formed in SBF or TRIS-buffered water. This is consistent with the Posner–Betts⁶⁰ structural model of ACP being built by aggregated $\text{Ca}_9(\text{PO}_4)_6$ clusters, with water molecules occupying their interstices. Our results confirm several observations from previous ^1H and ^{31}P MAS NMR studies on synthetic ACP,^{53,55} except for the presence of acidic protons in the structure, as either inferred from NMR^{58,59} or implied by “generalized” ACP stoichiometries.⁶¹

The present CPMAS results underscore the very similar $^1\text{H}-^{31}\text{P}$ contacts in synthetic and biomimetic hydroxyapatite as well as evidence closely related ^{31}P NMR characteristics of the CaP clusters in the S85 MBG relative to the ACP surface layer formed in vitro. The latter pair of phases exhibits similar degrees of structural disorder, as inferred from their comparable chemical shift-distributions, that is, ^{31}P NMR fwhm (see Figure 3 and Section 3.2). They also display identical $^1\text{H}-^{31}\text{P}$ contacts between their water and phosphate moieties.

The roughly twice as large T_{CP} values observed from the two ordered apatite structures (HA and HAref) relative to the amorphous phosphates (ACP and CaP) reflect a higher proton density in the latter. Equation 1 then implies the following relationship between the respective effective dipolar coupling constants

$$b_{\text{eff}}^{\text{ACP}} \approx \sqrt{2} b_{\text{eff}}^{\text{HA}}. \quad (7)$$

Equation 7 is consistent with a multitude of distinct $^1\text{H}-^{31}\text{P}$ coupling-topologies and may not provide detailed structural insight. However, H(C)A solely comprises OH groups, whereas water molecules constitute the proton source in the ACP structure (Figure 3); then, one plausible and *natural* structural scenario consistent with eq 7 is the replacement of each OH group in the apatite structure by one H_2O molecule (accompanied by removal of one Ca^{2+} ion) such that each shortest $^1\text{H}-^{31}\text{P}$ distance in apatite becomes two (nearly) equal heteronuclear distances in ACP. This provides a doubled proton density in the latter structure and the following stoichiometric relationship



where the left-hand side is formulated by assuming the “Posner cluster” as structural unit. Note that the postulated H_2O for OH substitutions naturally leads to the previously suggested (but thus far not proven) *interstitial* locations of the water molecules in ACP.^{60,61} We stress that whereas eq 8 is consistent with our

NMR data, it must not be taken too literally, and many other structural scenarios may also provide $^1\text{H}-^{31}\text{P}$ contacts obeying eq 7. Further work is required to (dis)prove the relationship eq 8.

4.3. NMR Relaxation Properties. For both ^1H and ^{31}P (Table 2), each very large relaxation time constant associated with the dominating NMR signal fraction observed from the two crystalline apatites, that is, HAref and the ordered phosphate component of tris16h, rationalizes the observed absence of ^{31}P signal-damping during CP (Figure 6 and Table 3). Furthermore, the markedly faster decays for both ^1H and ^{31}P of the amorphous phosphates, ACP in tris16h and CaP in S85, are also mirrored in their significantly lower values of $T_{1\rho}^{\text{H}}$ and $T_{1\rho}^{\text{P}}$, relative to HAref and H(C)A (Table 2). The main distinguishing property between the two amorphous components is the accelerated signal damping of the ^{31}P sites in the ACP phase of the tris16h sample, as compared with that of the CaP clusters of the pristine MBG. This likely stems from a higher mobility of the water molecules of biomimetic ACP relative to the CaP clusters present in the MBG pore walls. Káflak and Kolodziejski highlighted a strong dependence of the ^{31}P $T_{1\rho}$ relaxation on the “water” content in synthetic and biological apatites,³⁶ which correlates very well with our observed data.

Equation 3, which involves a $T_{1\rho}$ -driven NMR signal-decay also of ^{31}P , has to our knowledge hitherto only been noted recently in one related study in the context of crystalline calcium phosphates and bone.³⁶ In general, ^{31}P relaxation during spin-locking has been ignored in the analysis of $^1\text{H}-^{31}\text{P}$ CP-dynamics.^{35,37,38} Furthermore, the biexponential character of the ^{31}P relaxation generally observed from our samples has hitherto not been found from synthetic or biological apatites. However, previous reports^{35–38} typically employed CP during either static conditions or slower MAS rates than our experimentation carried out at 9.0 kHz, which may quench an otherwise active spin-diffusion. Yet, our T_{CP} values for the $\text{O}^1\text{H} \leftrightarrow ^{31}\text{PO}_4^{3-}$ and $^1\text{H}_2\text{O} \leftrightarrow ^{31}\text{PO}_4^{3-}$ contacts in the crystalline and amorphous phases agree well with the corresponding results observed from natural bone specimens by Maltsev et al.,³⁹ which were obtained at 12 kHz MAS.

Table 2 also lists the ^{31}P T_1 values obtained by saturation-recovery experimentation⁴⁸ from the S85, HAref, and tris16h samples. As previously reported,^{36,39,62} crystalline HA displays significantly faster spin–lattice NMR relaxation compared with the much less ordered apatite-like phosphate environments of bone and tooth, which Káflak and Kolodziejski attributed to the higher OH content present in HA relative to the natural tissues.³⁶ Interestingly, the amorphous (and OH-poor) CaP clusters of S85 indeed display much slower spin–lattice relaxation ($T_1^{\text{P}} = 128$ s; Table 2) compared with HAref ($T_1^{\text{P}} = 8.8$ s): the latter value agrees well with previous studies.^{36,62} Furthermore, the relaxation of the net

^{31}P NMR peak of the intermediately ordered phosphates in the *tris*16h and *sbfl*16h samples reveals T_1^{P} values of 79 ± 1 s and 96 ± 3 s, respectively. Hence, these time constants fall in-between those observed from the crystalline (HA_{ref}) and amorphous (CaP) structures, which supports the proposition that the spin–lattice relaxation is significantly influenced by the OH content in the structure.³⁶

5. CONCLUSIONS

We have investigated structural features of the phosphate environments in amorphous (ACP) and crystalline (HA) phases generated in vitro at the surface of an “S85” MBG of composition $\text{Ca}_{0.098}\text{Si}_{0.838}\text{P}_{0.064}\text{O}_{1.93}$. TEM/EDX results obtained from S85 before and after its soaking in SBF or TRIS-solutions for 16 h revealed a biomimetically grown surface layer of calcium phosphate comprising domains of nanocrystalline H(C)A. ^1H – ^{31}P 2D HETCOR NMR spectra recorded from these *sbfl*16h and *tris*16h specimens verified the coexistence of ACP and H(C)A: each respective component phase displayed the pairs of correlations $^1\text{H}_2\text{O} \leftrightarrow ^{31}\text{PO}_4^{3-}$ (ACP) and $\text{O}^1\text{H} \leftrightarrow ^{31}\text{PO}_4^{3-}$ (apatite), meaning that the orthophosphate ions are in close spatial proximity solely to water molecules and hydroxyl groups in the ACP and H(C)A phases, respectively. Neither our ACP formed in SBF nor TRIS-buffered water revealed any significant amounts of acidic protons.

The ^1H – ^{31}P CPMAS kinetics was monitored for each relevant $^{31}\text{PO}_4^{3-}$, O^1H , and $^1\text{H}_2\text{O}$ moiety in the S85 and *tris*16 h specimens as well as those in a synthetic HA sample HA_{ref}: we contrasted the underlying rate constants obtained by analyzing a series of NMR experiments involving variable contact intervals. Despite that the in-vitro-generated HA structure is less ordered than its HA_{ref} counterpart, both structures feature very closely related sets of ^1H – ^{31}P internuclear distances, as evidenced by their essentially identical rates of CP ^{31}P NMR signal growth. The structure of the two amorphous phases, biomimetic ACP and the CaP clusters of the MBG pore walls,^{28,44,45} is associated with a higher proton density originating from the presence of structural water molecules and resulting in twice as fast CP ^{31}P signal buildup relative to crystalline HA. This observation is consistent with a (simplified) structural scenario where each apatite OH group is replaced by one H_2O molecule (see eq 8).

The local and intermediate-range structure of the amorphous CaP clusters present in the pristine MBG is closely related to its biomimetic ACP counterpart, as evidenced by their shared ^1H and ^{31}P NMR characteristics in terms of (i) chemical shifts, implying very similar local electron densities at the ^{31}P sites; (ii) NMR peak widths, which translates into comparable structural (dis)order; and (iii) very similar (effective) ^1H – ^{31}P distances. These two amorphous phases mainly differ in their $T_{1\rho}$ relaxation properties, where ACP manifests significantly faster ^1H and ^{31}P NMR signal damping, likely reflecting a higher mobility of the water molecules in its structure relative to those of the CaP clusters. Furthermore, while sharing essentially all of their structural features with bulk ACP, the CaP clusters also comprise small amounts of the HA-characteristic OH groups (<5% of their total proton population).

AUTHOR INFORMATION

Corresponding Author

*E-mail: mattias.eden@mmk.su.se. Fax: +46 8 152187. Phone: +46 8 162375.

ACKNOWLEDGMENT

This work was supported by the Swedish Research Council (contracts VR-NT 2009-7551 and 2010-4943), the Faculty of Natural Sciences at Stockholm University, CICYT Spain (project MAT 2008-00736), and the Comunidad Autónoma de Madrid (project S2009/MAT-1472). P.N.G. was supported by a post-doctoral grant from the Carl Trygger Foundation. We thank Niklas Hedin for providing the hydroxyapatite reference sample.

REFERENCES

- (1) Lowenstam, H. A.; Weiner, S. *On Biomineralization*; Oxford University Press: New York, 1989.
- (2) Weiner, S.; Wagner, H. D. *Annu. Rev. Mater. Sci.* **1998**, *28*, 271–298.
- (3) Wise, E. R.; Maltsev, S.; Davies, M. E.; Duer, M. J.; Jäger, C.; Loveridge, N.; Murray, R. C.; Reid, D. G. *Chem. Mater.* **2007**, *19*, 5055–5057.
- (4) Hu, Y. Y.; Rawal, A.; Schmidt-Rohr, K. *Proc. Nat. Acad. Sci. U.S.A.* **2010**, *107*, 22425–22429.
- (5) Dorozhkin, S. V. *Materials* **2009**, *2*, 399–498.
- (6) Hench, L. L. *J. Am. Ceram. Soc.* **1991**, *74*, 1487–1510.
- (7) Vallet-Regí, M.; Ragel, C. V.; Salinas, A. J. *Eur. J. Inorg. Chem.* **2003**, 1029–1042.
- (8) Arcos, D.; Vallet-Regí, M. *Acta Biomater.* **2010**, *6*, 2874–2888.
- (9) Hench, L. L.; Polak, J. M. *Science* **2002**, *295*, 1014–1017.
- (10) Rahaman, M. N.; Day, D. E.; Sonny Bal, B.; Fu, Q.; Jung, S. B.; Bonewald, L. F.; Tomsia, A. P. *Acta Biomater.* **2011**, *7*, 2355–2373.
- (11) Ogino, M.; Hench, L. L. *J. Non-Cryst. Solids* **1980**, *38/39*, 673–678.
- (12) Kim, C. Y.; Clark, A. E.; Hench, L. L. *J. Non-Cryst. Solids* **1989**, *113*, 195–202.
- (13) Ebisawa, Y.; Kokubo, T.; Ohura, K.; Yamamuro, T. *J. Mater. Sci. Mater. Med.* **1990**, *1*, 239–244.
- (14) Andersson, Ö. H.; Karlsson, K. H. *J. Non-Cryst. Solids* **1991**, *129*, 145–151.
- (15) Ohtsuki, C.; Kokubo, T.; Yamamuro, T. *J. Non-Cryst. Solids* **1992**, *143*, 84–92.
- (16) Vallet-Regí, M.; Pérez-Pariente, J.; Izquierdo-Barba, I.; Salinas, A. J. *Chem. Mater.* **2000**, *12*, 3770–3775.
- (17) Takadama, H.; Kim, H. M.; Kokubo, T.; Nakamura, T. *Chem. Mater.* **2001**, *13*, 1108–1113.
- (18) Salinas, A. J.; Martin, A. I.; Vallet-Regí, M. *J. Biomed. Mater. Res., Part A* **2002**, *61*, 524–532.
- (19) Saravanapavan, P.; Jones, J. R.; Pryce, R. S.; Hench, L. L. *J. Biomed. Mater. Res., Part A* **2003**, *66*, 110–119.
- (20) Banchet, V.; Jallot, E.; Michel, J.; Wortham, L.; Laurent-Maquin, D.; Balossier, G. *Surf. Interface Anal.* **2004**, *36*, 658–665.
- (21) Yan, X. X.; Yu, C. Z.; Zhou, X. F.; Tang, J. W.; Zhao, D. Y. *Angew. Chem., Int. Ed.* **2004**, *43*, 5980–5984.
- (22) Yan, X. X.; Huang, X. H.; Yu, C. Z.; Deng, H. X.; Wang, Y.; Zhang, Z. D.; Qiao, S. Z.; Lu, G. Q.; Zhao, D. Y. *Biomaterials* **2006**, *27*, 3396–3403.
- (23) López-Noriega, A.; Arcos, D.; Izquierdo-Barba, I.; Sakamoto, Y.; Terasaki, O.; Vallet-Regí, M. *Chem. Mater.* **2006**, *18*, 3137–3144.
- (24) Hayakawa, S.; Tsuru, K.; Ohtsuki, C.; Osaka, A. *J. Am. Ceram. Soc.* **1999**, *82*, 2155–2160.
- (25) Lin, K. S. K.; Tseng, Y. H.; Mou, Y.; Hsu, Y. C.; Yang, C. M.; Chan, J. C. C. *Chem. Mater.* **2005**, *17*, 4493–4501.
- (26) Skipper, L. J.; Sowrey, F. E.; Rashid, R.; Newport, R. J.; Lin, Z.; Smith, M. E. *Phys. Chem. Glasses* **2005**, *46*, 372–376.
- (27) Dietrich, E.; Oudadesse, H.; Le Floch, M.; Bureau, B.; Gloriant, T. *Adv. Eng. Mater.* **2009**, *11*, B98–B105.
- (28) Gunawidjaja, P. N.; Lo, A. Y. H.; Izquierdo-Barba, I.; García, A.; Arcos, D.; Stevansson, B.; Grins, J.; Vallet-Regí, M.; Edén, M. *J. Phys. Chem. C* **2010**, *114*, 19345–19356.

- (29) Gunawidjaja, P. N.; Izquierdo-Barba, I.; Mathew, R.; Jansson, K.; García, A.; Grins, J.; Arcos, D.; Vallet-Regí, M.; Edén, M. **2011**, submitted.
- (30) Beshah, K.; Rey, C.; Glimcher, M. J.; Schimizu, M.; Griffin, R. G. *J. Solid. State. Chem.* **1990**, *84*, 71–81.
- (31) Santos, R. A.; Wind, R. A.; Bronnimann, C. E. *J. Magn. Reson., Ser. B* **1994**, *105*, 183–187.
- (32) Rey, C.; Kim, H. M.; Gerstenfeld, L.; Glimcher, M. J. *J. Bone Miner. Res.* **1995**, *10*, 1577–1588.
- (33) Wu, Y. T.; Ackerman, J. L.; Kim, H. M.; Rey, C.; Barroug, A.; Glimcher, M. J. *J. Bone Miner. Res.* **2002**, *17*, 472–480.
- (34) Cho, G. Y.; Wu, Y. T.; Ackerman, J. L. *Science* **2003**, *300*, 1123–1127.
- (35) Kaflak-Hachulska, A.; Samoson, A.; Kolodziejski, W. *Calcif. Tissue Int.* **2003**, *73*, 476–486.
- (36) Kaflak, A.; Kolodziejski, W. *Solid State Nucl. Magn. Reson.* **2007**, *31*, 174–183.
- (37) Kolmas, J.; Kolodziejski, W. *Chem. Commun.* **2007**, 4390–4392.
- (38) Kaflak, A.; Kolodziejski, W. *Magn. Reson. Chem.* **2008**, *46*, 335–341.
- (39) Maltsev, S.; Duer, M. J.; Murray, R. C.; Jäger, C. *J. Mater. Sci.* **2007**, *42*, 8804–8810.
- (40) Wilson, E. E.; Awonusi, A.; Morris, M. D.; Kohn, D. H.; Tecklenburg, M. M. J.; Beck, L. W. *Biophys. J.* **2006**, *90*, 3722–3731.
- (41) Huang, S. J.; Tsai, Y. L.; Lee, Y. L.; Lin, C. P.; Chan, J. C. C. *Chem. Mater.* **2009**, *21*, 2583–2585.
- (42) Laurencin, D.; Wong, A.; Chrzanowski, W.; Knowles, J. C.; Qiu, D.; Pickup, D. M.; Newport, R. J.; Gan, Z. H.; Duer, M. J.; Smith, M. E. *Phys. Chem. Chem. Phys.* **2010**, *12*, 1081–1091.
- (43) Kokubo, T.; Kushitani, H.; Sakka, S.; Kitsugi, T.; Yamamuro, T. *J. Biomed. Mater. Res.* **1990**, *24*, 721–734.
- (44) Leonova, E.; Izquierdo-Barba, I.; Arcos, D.; Lopez-Noriega, A.; Hedin, N.; Vallet-Regí, M.; Edén, M. *J. Phys. Chem. C* **2008**, *112*, 5552–5562.
- (45) García, A.; Cicuéndez, M.; Izquierdo-Barba, I.; Arcos, D.; Vallet-Regí, M. *Chem. Mater.* **2009**, *21*, 5474–5484.
- (46) Brinker, C. J.; Lu, Y. F.; Sellinger, A.; Fan, H. Y. *Adv. Mater.* **1999**, *11*, 579–585.
- (47) Levitt, M. H. *J. Magn. Reson.* **1997**, *126*, 164–182.
- (48) Ernst, R. R.; Bodenhausen, G.; Wokaun, A. *Principles of Nuclear Magnetic Resonance in One and Two Dimensions*; Clarendon Press: Oxford, U.K., 1987.
- (49) Metz, G.; Wu, X. L.; Smith, S. O. *J. Magn. Reson., Ser. A* **1994**, *110*, 219–227.
- (50) Alemany, L. B.; Grant, D. M.; Pugmire, R. J.; Alger, T. D.; Zilm, K. W. *J. Am. Chem. Soc.* **1983**, *105*, 2133–2141.
- (51) Kolodziejski, W.; Klinowski, J. *Chem. Rev.* **2002**, *102*, 613–628.
- (52) Ladizhansky, V.; Vega, S. *J. Chem. Phys.* **2000**, *112*, 7158–7168.
- (53) Tropp, J.; Blumenthal, N. C.; Waugh, J. S. *J. Am. Chem. Soc.* **1983**, *105*, 22–26.
- (54) Aue, W. P.; Roufosse, A. H.; Glimcher, M. J.; Griffin, R. G. *Biochemistry* **1984**, *23*, 6110–6114.
- (55) Belton, P. S.; Harris, R. K.; Wilkes, P. J. *J. Phys. Chem. Solids* **1988**, *49*, 21–27.
- (56) Isobe, T.; Nakamura, S.; Nemoto, R.; Senna, M.; Sfihi, H. *J. Phys. Chem. B* **2002**, *106*, 5169–5176.
- (57) Jäger, C.; Welzel, T.; Meyer-Zaika, W.; Eppel, M. *Magn. Reson. Chem.* **2006**, *44*, 573–580.
- (58) Roberts, J. E.; Heughebaert, M.; Heughebaert, J. C.; Bonar, L. C.; Glimcher, M. J.; Griffin, R. G. *Calcif. Tissue Int.* **1991**, *49*, 378–382.
- (59) Jäger, C.; Maltsev, S.; Karrasch, A. In *Bioceramics. Volume 18; Proceedings of the 18th International Symposium on Ceramics in Medicine: The Annual Meeting of the International Society for Ceramics in Medicine (ISCM)*, Kyoto, Japan, Dec 5–8, 2005; Nakamura, T., Yamashita, K., Neo, M., Eds.; Trans Tech Publications: Enfield, NH, **2006**; Vol. 309–311, pp 69–72.
- (60) Posner, A. S.; Betts, F. *Acc. Chem. Res.* **1975**, *8*, 273–281.
- (61) Dorozhkin, S. V. *Acta Biomater.* **2010**, *6*, 4457–4475.
- (62) Rothwell, W. P.; Waugh, J. S.; Yesinowski, J. P. *J. Am. Chem. Soc.* **1980**, *102*, 2637–2643.